To Survive or To Shatter: The Impact of Cosmic Rays on the Fate of Stripped Cold Clouds

The Astrophysical Journal, 1004:147 (17pp), 2026 June 20 https://doi.org/10.3847/1538-4357/ae664f

To Survive or To Shatter: The Impact of Cosmic Rays on the Fate of Stripped Cold Clouds

Manami Roy[1,2], Kung-Yi Su[3,4], Stephanie Tonnesen[5], Yue Samuel Lu[6,7], Cameron Hummels[8], and Sam B. Ponnada[9]

[1] Center for Cosmology and Astro Particle Physics (CCAPP), The Ohio State University, 191 W. Woodruff Avenue, Columbus, OH 43210, USA; roy.516@osu.edu
[2] Department of Astronomy, The Ohio State University, 140 W. 18th Ave., Columbus, OH 43210, USA
[3] Black Hole Initiative, Harvard University, 20 Garden St., Cambridge, MA 02138, USA
[4] Department of Physics and Astronomy and CIERA, Northwestern University, 2145 Sheridan Road, Evanston, IL 60208, USA
[5] Center for Computational Astrophysics, Flatiron Institute, 162 5th Ave, New York, NY 10010, USA
[6] Department of Astronomy and Astrophysics, University of California, San Diego, La Jolla, CA 92093, USA
[7] Physics Department, University of California, San Diego, La Jolla, CA 92093, USA
[8] TAPIR, California Institute of Technology, Pasadena, CA 91125, USA
[9] Department of Physics and Astronomy, Chalmers University of Technology, SE-412 96 Gothenburg, Sweden
Received 2025 September 19; revised 2026 April 20; accepted 2026 April 25; published 2026 June 10

Abstract

Does cosmic-ray (CR) pressure matter for the circumgalactic medium (CGM)? While prior studies suggest that CRs influence the thermal and dynamical state of the CGM, their overall importance remains an open question due to limited observational constraints and the strong dependence of simulation predictions on the implementation of CR physics. In the context of the multiphase CGM, the role of CRs remains underexplored, especially in governing the formation and survival of cold gas clouds and structures that are expected to fuel future star formation in the host galaxy. We investigate how CRs affect ram-pressure-stripped cold gas clouds originating from satellite galaxies in a Milky Way–like halo. Using high-resolution simulations with varying CR energy densities, we find that CRs can significantly modify the size and survival of stripped clouds. Specifically, CR pressure "puffs up" cold clouds, increasing their surface area and enabling more efficient mixing-layer cooling, which allows them to grow in mass. This enhanced growth results in higher cold gas inflow rates into the central galaxy, leading to an increased star formation rate compared to the no-CR case at later times. Moreover, CRs can boost the total cold gas mass in the CGM by up to a factor of 4. These effects are most pronounced in simulations where the CR energy density is in equipartition with the thermal gas. We show that CRs can play a critical role in regulating the cold phase of the CGM contributed by satellites, and therefore their ability to feed galaxies.

Unified Astronomy Thesaurus concepts: Circumgalactic medium (1879); Cosmic rays (329); Galaxy evolution (594)

1. Introduction

The diffuse gaseous halo surrounding a galaxy, known as the circumgalactic medium (CGM), acts as a crucial interface between the galactic disk and the intergalactic medium (IGM; see J. Tumlinson et al. 2017; C.-A. Faucher-Giguère & S. P. Oh 2023 for reviews). The CGM is multiphase and contains a substantial reservoir of cold gas ($T < 10^4$ K), which accounts for up to ∼30%–50% of a galaxy's total baryonic matter (J. K. Werk et al. 2014). The cold phase of the CGM is thought to be an important source of star formation fuel, as it can accrete onto the galactic disk and sustain ongoing star formation. Understanding the origin, survival, and transport of this cold gas is therefore crucial for constructing a comprehensive picture of galaxy evolution. However, key questions about this cold phase remain unanswered in the field. How does this gas accumulate in the outer regions of the CGM (e.g., J. Tumlinson et al. 2013; B. A. Keeney et al. 2018)? Why do quenched galaxies, which no longer form stars, still harbor large reservoirs of cold gas (e.g., M. A. Berg et al. 2019)? And why do Cosmic Origins Spectrograph-Halos observations suggest that the density of this cold gas is an order of magnitude lower than expected if it were in thermal pressure equilibrium with the surrounding hot gas (J. K. Werk et al. 2014)?

These questions have sparked significant interest and speculation in recent years. Two primary scenarios have been proposed to explain the origin of cold gas in the CGM: either the cold gas originates ex situ, e.g., in galactic disks, satellite galaxies, or the IGM (e.g., M. Gronke & S. P. Oh 2018; D. B. Fielding et al. 2020; M. Li & S. Tonnesen 2020; M. Roy et al. 2024) and is subsequently transported into the halo, or it forms in situ, through cooling and condensation processes within the CGM itself (e.g., M. McCourt et al. 2011; P. Sharma et al. 2012; G. M. Voit et al. 2015; M. Roy et al. 2021). Satellite galaxies can contribute substantial amounts of cold gas to the CGM through both ram pressure stripping and induced cooling in the mixing layers of stripped gas, with both mechanisms likely playing comparable roles (M. Roy et al. 2024; M. Damle et al. 2025). Cold gas in the CGM can also form in situ via thermal instability, wherein small perturbations in hot, gravitationally stratified gas trigger runaway cooling and condensation. This process, initially proposed in the context of galaxy clusters, is now recognized as an important mechanism for generating cold CGM gas (e.g.,

M. McCourt et al. 2011; P. Sharma et al. 2012; G. M. Voit et al. 2015) and regulating the baryon cycle.

Therefore, both in situ formation and external transport contribute to the presence of cold gas in the CGM, though their relative importance varies across galaxies. While cold gas is expected to be short-lived in the hot halo environment (e.g., C. F. McKee & L. L. Cowie 1975; D. Zhang et al. 2017), observations of multiphase outflows (e.g., T. Ashley et al. 2020; A. Fluetsch et al. 2021) and recent theoretical works (e.g., M. Gronke & S. P. Oh 2018; D. B. Fielding et al. 2020; M. Li & S. Tonnesen 2020) suggest that cold gas can survive and even grow in hot winds. However, it remains uncertain whether these mechanisms can fully account for the observed cold gas mass in the CGM.

The influence of cosmic rays (CRs) on cold gas has been investigated in only a few studies. P. Sharma et al. (2010) suggested that adiabatic CRs can suppress cold gas formation by reducing the growth of thermal instabilities. I. S. Butsky et al. (2020) also showed that CRs can influence thermal-instability-driven formation of cold gas by providing non-thermal pressure support. This additional pressure reduces the compressibility of the gas, enabling it to cool at lower densities and leading to the formation of larger cold structures. Their simulations, which include CR physics, often produce extended cold gas clouds or mistlike configurations, in contrast to the small, dense cloudlets typically formed in their absence. In some cases, they find that CR pressure can increase the cold gas mass in the halo by inhibiting the inward precipitation of condensed gas toward the galactic center. However, the impact of CRs on this ex situ cold phase originating from satellites or the IGM remains largely unexplored.

In this paper, we investigate the impact of CRs on ram pressure stripping and address the following key questions: Do CRs affect the stripping rate of satellite galaxies? What role do CRs play in determining the mass and size of stripped cold clouds? And do CRs impact the survival of cold clouds and their subsequent infall and feeding of the central galaxy? In Section 2, we discuss the methodology of our simulation, including the initial conditions (Section 2.1) and our definition of cold CGM gas used in the analysis (Section 2.2). In Section 3, we present the results from our analysis of the simulations, focusing on the size and mass distribution of ram-pressure-stripped clouds (Section 3.2), cloud mass (Section 3.3), the covering fraction of cold CGM gas (Section 3.4) and its inflow rate (Section 3.5). We discuss the role of CR physics in Section 4. To conclude, we summarize our results and outline future work in Section 5.

2. Methodology

We perform our simulations using the GIZMO code (P. F. Hopkins 2015),[10] operating in its meshless finite mass (MFM) mode. This Lagrangian, mesh-free Godunov method combines the strengths of both smoothed-particle hydrodynamics (SPH) and grid-based techniques. The numerical framework and validation tests are described in a series of associated papers. These include implementations of hydrodynamics and self-gravity (P. F. Hopkins 2015), magnetohydrodynamics (MHD; P. F. Hopkins 2016; P. F. Hopkins & M. J. Raives 2016), anisotropic conduction and viscosity (P. F. Hopkins 2017; K.-Y. Su et al. 2017), and CRs (T. K. Chan et al. 2019).

All simulations implement the Feedback in Realistic Environments 2 (FIRE-2) model,[11] which provides a comprehensive treatment of the multiphase interstellar medium (ISM), star formation, and stellar feedback (P. F. Hopkins et al. 2018a, 2018b). Gas cooling is modeled over a wide temperature range (10–10^{10} K), accounting for processes such as photoelectric and photoionization heating, collisional and Compton cooling, atomic and molecular transitions, fine-structure emission, and recombination.

Star formation is modeled using sink particles that form only in dense, molecular gas regions exceeding $100\,\mathrm{cm}^{-3}$, where local self-gravity and self-shielding dominate. Newly formed star particles inherit the metallicity of their progenitor gas and represent single-age stellar populations. Stellar feedback is implemented based on initial mass function (IMF)-averaged quantities derived from STARBURST99 (C. Leitherer et al. 1999), assuming a Kroupa IMF (P. Kroupa 2002).

The feedback model includes multiple physical channels: radiative feedback, including photoionization, photoelectric heating, and radiation pressure (single and multiple scattering), tracked across five spectral bands (ionizing, far-UV, near-UV, optical–near-IR, and IR); stellar winds, accounting for mass, energy, momentum, and metal injection into the ISM from OB and asymptotic giant branch stars; and supernovae (SNe) feedback from both Type II and Ia SNe, including prompt and delayed explosions, with corresponding thermal and kinetic energy, mass, and metal injection into the surrounding ISM. All simulations incorporate MHD, fully anisotropic thermal conduction and viscosity using Spitzer–Braginskii coefficients.

For simulations with CRs, we include anisotropic streaming and diffusion along magnetic field lines. CR streaming occurs at the local Alfvén speed, including a corresponding streaming loss term that thermalizes the energy, as described in M. Uhlig et al. (2012). CR diffusion is modeled using a constant parallel (anisotropic) diffusivity of $\sim 10^{29}\,\mathrm{cm}^2\,\mathrm{s}^{-1}$ in our fiducial run, coupled with adiabatic exchanges with the thermal gas and energy losses via Coulomb and hadronic interactions (F. Guo & S. P. Oh 2008). We model a single GeV energy bin of CR protons, appropriate for the dominant CR pressure component, and treat CRs as ultrarelativistic particles. CRs are injected by SNe, with 10% of the explosion energy allocated to CRs, consistent with previous studies (C. Pfrommer et al. 2017a, 2017b). Additional implementation details and physical modeling of CRs are described in K.-Y. Su et al. (2019), T. K. Chan et al. (2019), and P. F. Hopkins et al. (2020).

In this study, we focus exclusively on the m12 host halo, representing a Milky Way (MW)–mass galaxy with a total mass of approximately $1.8 \times 10^{12}\,M_\odot$, along with either two or 20 satellite galaxies embedded in dark matter (DM) halos of $2 \times 10^{10}\,M_\odot$ (denoted as m10) and $2 \times 10^{9}\,M_\odot$ (denoted as m09), respectively. The mass resolution for the low-resolution runs of m09 and m10 (as well as m12) is 4×10^4 and 8×10^4 $M_\odot$, respectively, while the high-resolution runs attain 8×10^3 $M_\odot$. The minimum gravitational force softening for gas is 1 pc,

[10] Publicly available at GIZMO: https://github.com/pfhopkins/gizmo-public.

[11] Although the mass of our host galaxy is comparable to that of the m12i FIRE-2 cosmological simulation, our setup is entirely idealized and employs different initial conditions. Therefore, a direct comparison with the cosmological FIRE-2 results is not appropriate.

Table 1
Summary of All Runs: m09: (20 m09 Satellites) and m10 (Two m10 Satellites)

Set (1)	Symbol (2)	Resolution (3)	$P_{th,ini}/P_{tot,ini}$ (4)	$P_{CR,ini}/P_{tot,ini}$ (5)	D (6)	β_{ini} (7)
1. Fiducial m09 runs	m09_noCR	Low	1	0	No	Profile
	m09_noCR_hr	High	1	0	No	Profile
	m09_CR_l_hr	High	1	Profile	D29	Profile
	m09_CR_l	Low	1	Profile	D29	Profile
	m09_CR_m1	Low	9/10	1/10	D29	Profile
	m09_CR_m2	Low	3/4	1/4	D29	Profile
	m09_CR_h	Low	2/3	1/3	D29	Profile
2. Fiducial m10 runs	m10_noCR	Low	1	0	No	Profile
	m10_CR_l	Low	1	Profile	D29	Profile
	m10_CR_m1	Low	9/10	1/10	D29	Profile
	m10_CR_m2	Low	3/4	1/4	D29	Profile
	m10_CR_h	Low	2/3	1/3	D29	Profile
3. Other m09 runs	m09_CR_h_D28	Low	2/3	1/3	D28	Profile
	m09_CR_h_beta300	Low	2/3	1/3	D29	300
	m09_CR_m2_overP	Low	1	1/4	D29	Profile
	m09_noCR_underP	Low	3/4	0	No	Profile
	m09_CR_m2_underP	Low	1/2	1/4	D29	Profile

Note. We summarize the symbols of the runs used throughout the paper in Column (2). We indicate the resolution of the runs in Column (3), where the mass resolution for the low-resolution m09 and m10 runs is 4×10^4 and $8 \times 10^4\ M_\odot$, respectively, while all high-resolution runs have a mass resolution of $8 \times 10^3\ M_\odot$. In Columns (4), (5), and (7), we list the initial thermal pressure fraction, CR pressure fraction, and $\beta = P_{th}/P_B$, respectively. The anisotropic diffusion coefficient used in each run is given in Column (6), where D29 denotes $D = 10^{29}$ cm^2 s^{-1} and D28 denotes $D = 10^{28}$ cm^2 s^{-1}.

which is adaptive and matched to the hydrodynamic resolution. We discuss our resolution study in Appendix A.

2.1. Initial Conditions

Our initial setup follows the methodology described in K.-Y. Su et al. (2019), M. Roy et al. (2024), and M. Roy et al. (2025). To ensure a stable and quasi-equilibrium CGM environment for the host galaxy, the simulation domain is extended to 3 times the virial radius of the host halo. The system is then evolved adiabatically (i.e., without radiative cooling or star formation) for 4.5 Gyr to allow any initial transients to relax before introducing satellite galaxies. We initially place the m10 satellite galaxies at radii of 100 and 150 kpc, and distribute the m09 satellites randomly between 100 and 150 kpc on circular orbits.[12] Simulation parameters and detailed properties are provided in Table 1. The m09 satellites have a gas mass of $7 \times 10^7\ M_\odot$ and a gas disk radius of 0.87 kpc, while the m10 satellites have a gas mass of $4.2 \times 10^8\ M_\odot$ and a gas disk radius of 2.1 kpc. Other galaxy properties, like stellar mass and total baryonic mass, can be found in Table 1 of M. Roy et al. (2024).

We initialize the DM halo, stellar bulge, central black hole, and gas+stellar disk of the m12 galaxy following the methodology outlined in V. Springel & S. D. M. White (1999) and V. Springel (2000). The initial gas metallicity decreases radially from solar ($Z = 0.02$) to $Z = 0.001$, following the profile

$$Z(r) = 0.02\left(0.05 + \frac{0.95}{1 + (r/20\ \text{kpc})^{1.5}}\right). \tag{1}$$

The initial metallicities of the satellites are set to match the host halo's CGM metallicity at their starting locations. Magnetic fields are initialized in the azimuthal direction with a radial dependence

$$|\boldsymbol{B}(r)| = \frac{0.03\ \mu\text{G}}{1 + (r/20\ \text{kpc})^{0.375}}. \tag{2}$$

The initial β values in our "profile" runs range from 10^3 to 10^6. Although we start with a high initial β value for the magnetic field, it evolves to a more physical configuration, reaching β values of $\sim$10 within the inner few kiloparsecs of the disk midplane, consistent with recent CHANG-ES results (M. Krause et al. 2018). We also discuss in Section 4 how an increase in the initial magnetic field affects our results. Further details of the initial setup can be found in the Methodology section of M. Roy et al. (2024).

For simulations that include CRs, we adopt three different initialization schemes. In the high-CR runs (`CR_h`), the CR energy density is initialized in equipartition with the thermal energy density. To preserve the total pressure and maintain hydrostatic equilibrium, we reduce the initial gas temperature by two-thirds and allocate the remaining energy to CRs. In the mid-CR runs (`CR_m1,2`), CRs are initialized at one-tenth and one-quarter of the thermal energy. In the low-CR runs (`CR_l`), CRs are initialized such that the CR energy density is in equipartition with the magnetic energy density, which is approximately 5 orders of magnitude lower than the thermal energy density. In Table 1, we list all of our runs with a full description of their initial pressure and CR transport

[12] Since the satellite masses are 2 orders of magnitude smaller than that of the host halo, their instantaneous introduction into the CGM does not significantly perturb the ambient medium. This is illustrated by the sub-unity Mach numbers in the CGM shown in M. Roy et al. (2024), which indicate subsonic velocity dispersion in the CGM of the host galaxy with the inclusion of different satellite distributions.

parameters, including the diffusion coefficient and magnetic field configuration.

2.2. Definition and Classification of Cold Circumgalactic Medium Gas

In this section, we describe all of our definitions used to classify cold gas throughout the simulation. We note that they are the same as in M. Roy et al. (2024) and have been tested extensively for their robustness.

1. *Cold gas.* To identify the cold phase of the CGM in our simulation, we adopt a temperature threshold of $T < 3 \times 10^4$ K.
2. *CGM and ISM boundary.* To focus exclusively on the CGM and exclude the ISM of the central galaxy, we remove from our analysis all gas within 40 kpc (approximately 0.15 $R_{\rm vir}$) of the host galaxy's center.
3. *Satellite boundary.* To define the spatial extent of a satellite's influence, we consider the decline in its gas surface density, given by $\Sigma = \Sigma_0\, e^{-r/r_d}$, where r_d is the stellar scale radius. The gas scale radius is defined as $r_{\rm gd} \sim 2.7\, r_d$, beyond which Σ drops significantly (A. V. Kravtsov 2013). We define a radius of 6 $r_{\rm gd}$ from the satellite center (identified with the coordinates of its central black hole) as the boundary beyond which the satellite's gravitational influence on the surrounding gas becomes negligible.

We further distinguish between different origins of cold gas using the Lagrangian MFM method implemented in the GIZMO code, which allows us to track individual gas particles across the simulation. This enables us to classify cold gas based on both its thermal evolution and its dynamical interaction with satellite galaxies. Using this framework, we classify cold gas in the CGM into four categories:

1. *Cold gas inside the satellite (sat).* Gas particles that originate within the satellite and remain within 6 $r_{\rm gd}$.
2. *Stripped cold gas (sat −> host).* Gas particles that originate within the satellite but move beyond 6 $r_{\rm gd}$ while remaining below 3×10^4 K. These particles are considered to be cold gas stripped from the satellite.
3. *Host gas cooled inside the satellite (host −> sat).* Gas particles initially associated with the host CGM that cool to $T < 3 \times 10^4$ K and move to within the satellite's effective radius ($r < 6\, r_{\rm gd}$). This refers to hot gas from the host halo that enters the satellite's gravitational potential well and subsequently cools within it.
4. *Host gas cooled outside the satellite (host).* Gas particles that begin as host CGM and cool below 3×10^4 K without ever entering the satellite's defined boundary. This is the host halo gas that undergoes cooling outside the satellite, either within mixing layers of stripped cold gas or due to turbulence-induced cooling.

In summary, we define the cold CGM using a combination of temperature thresholds, spatial cuts, and particle tracking. This allows us to isolate gas cooled by different origins, setting the stage for the quantitative analysis in the next section.

3. Results

The primary objective of this paper is to investigate the impact of CRs on the cold gas in the CGM that has been stripped from satellite galaxies by ram pressure in a MW-like host halo. We begin by presenting visual insights from simulation snapshots to build physical intuition, followed by a quantitative analysis of the cold gas mass, size, and evolution under the influence of CRs. We restrict our analysis up to and including the snapshot at 2.0 Gyr, which corresponds to the survival time of cold stripped gas from the m09 satellites in the host CGM. We note that the trends observed for the m10 satellites beyond 2 Gyr remain consistent with those presented at earlier times.

3.1. How Do Cosmic Rays Affect Ram-pressure-stripped Cold Clouds?

In this section, we present an overview of the CGM gas evolution in the host galaxy using temperature snapshots at 1 Gyr from a suite of simulations. In Figure 1, we show edge-on projections of the temperature distribution for two satellite systems—`m10` (top panels) and `m09` (bottom panels)—under varying CR content. The CR energy density increases from left to right across the panels, with the leftmost column representing the no-CR case and the rightmost corresponding to the highest CR energy density.

To generate these maps, we interpolate the gas particle data onto a uniform 512^3 grid using a smoothing kernel based on each particle's smoothing length, following a standard SPH-like deposition method. During deposition, temperature values are mass weighted within each grid cell. For the final projection, we apply an n^2 weighting along the line of sight, roughly corresponding to a luminosity-weighted temperature map.

We differentiate between gas originating from satellites and that from the host using the satellite fraction parameter, $f_{\rm sat}$. This quantity is computed as a mass-weighted average along the projection axis, excluding gas associated with the host ISM and particles with temperatures exceeding 3×10^5 K. A value of $f_{\rm sat} = 1$ indicates purely satellite-origin gas, while $f_{\rm sat} = 0$ denotes purely host-origin gas. In the visualizations, temperature is encoded through color saturation. All panels are centered on the host galaxy, and the thin blue strip at the center (0, 0) represents the cold ISM of the host.

The similarity of this snapshot across the different runs indicates that all simulations tell a similar general story. Initially, cold gas is primarily confined to satellites, with short trailing tails. Over time, these tails lengthen as cold gas escapes the satellites' gravitational influence and moves toward the central galaxy. Increasing mixing with the host CGM is reflected by a color shift from red to orange. Cold gas is predominantly located near the central regions of the satellites, in outflow regions, or along stripped tails. The satellite fraction $f_{\rm sat}$ decreases smoothly along these tails, indicating progressive mixing. Much of this cooled gas spatially coincides with the stripped cold gas and appears orange in color, suggesting significant mixing between the two components. Moreover, the stripped cold gas clouds are larger in simulations with the more massive m10 satellites than in the lower-mass m09 systems.

This visual comparison serves as an initial step in understanding the influence of CRs on the cold gas in the CGM.

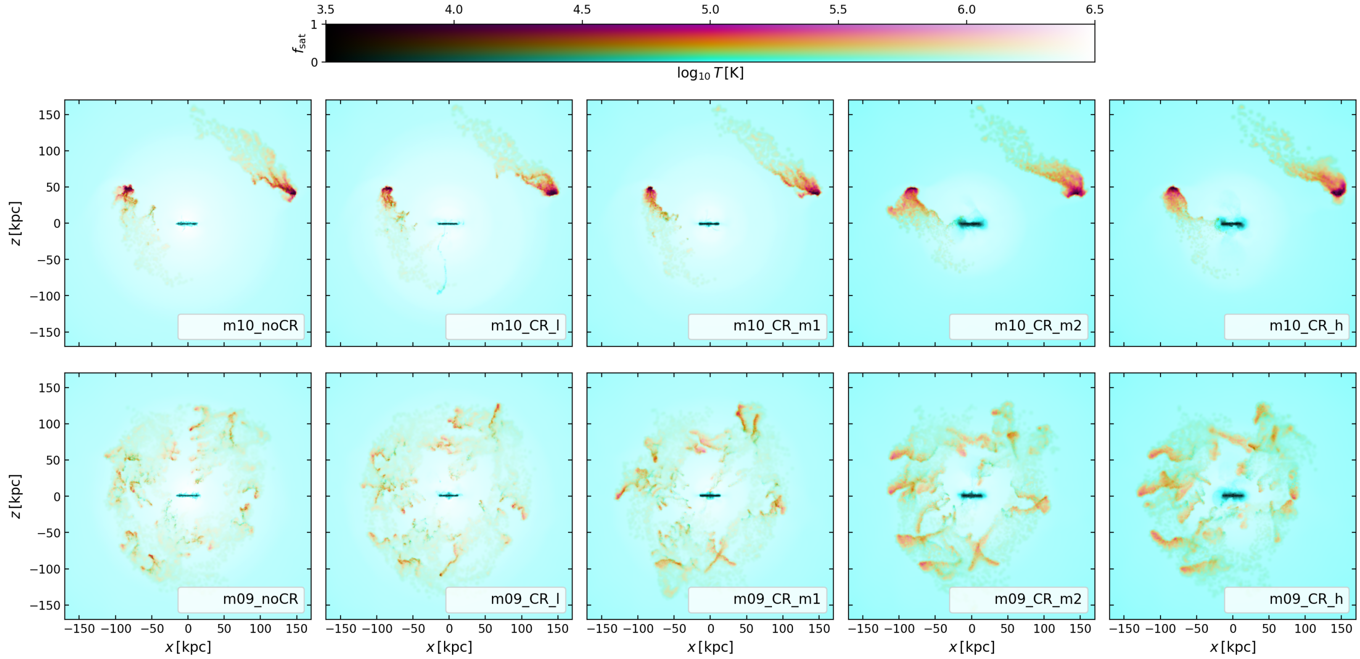

Figure 1. Temperature distributions for different simulations (see Table 1) at $t = 1$ Gyr. The color bar varies in both color and saturation based on f_{sat} and temperature, respectively. The parameter f_{sat} represents the local mass fraction originating from the satellite, such that $f_{sat} = 1$ corresponds to purely satellite gas and $f_{sat} = 0$ corresponds to purely host gas. The stripped cold gas streams behind the satellites and falls toward the central disk. Cool gas is also induced in the mixing layer between the stripped cool gas and the hot host gas. The top and bottom panels show the m10 and m09 runs, respectively. In each row, the CR content increases from left to right, with the leftmost panel corresponding to the no-CR case and the rightmost panel corresponding to the highest CR content. From left to right, the ram-pressure-stripped clouds become larger and more extended as the CR content increases.

With increasing CR content, the cold gas structures become more coherent and extended, exhibiting larger surface areas. This effect is particularly evident in the m09 simulations with smaller clouds: By $t = 1$ Gyr, the cold clouds in the no-CR runs are almost entirely disrupted and mixed with the CGM, whereas those in the high- (h) and mid- (m2) CR runs retain their structural integrity. A similar trend is observed for the m10 satellites: Cold gas stripped from the nearest satellite is nearly dissolved in the no-CR case but remains intact in the high- (h) and mid- (m2) CR scenarios. Even for the more distant m10 satellite, the presence of CRs leads to a visibly larger and more inflated ram-pressure-stripped tail, while in the absence of CRs, the tail is composed of narrower filaments, suggesting enhanced destruction of cold gas. The snapshots also reveal more mixing-layer cooling (indicated by the orange color) within the host CGM in the high-CR runs than in the no-CR runs, likely due to the larger cloud surface areas. Consequently, these clouds grow more substantially under the influence of CRs.

In summary, CRs appear to significantly influence the size and survival of ram-pressure-stripped cold gas in the CGM. Higher CR content leads to larger, more coherent cold gas clouds that resist mixing and survive longer. In the following sections, we quantitatively confirm our visual interpretation that CRs enhance mixing-layer cooling by increasing the cloud surface area.

3.2. Do Cosmic Rays Affect the Size of the Clouds?

Motivated by the trends observed in the visual inspection, we proceed to quantitatively assess the mass and size of the cold gas clouds identified in each simulation. To this end, we apply a Friends-of-Friends (FoF) algorithm to the gas particles. Cold gas particles are defined using a temperature threshold of $T < 3 \times 10^4$ K. For cloud identification, we adopt a linking length of 2 kpc and require a minimum of 10 particles per group. Thus, any collection of at least 10 cold particles connected within a 2 kpc linking length is identified as a coherent cold gas cloud. Additionally, we restrict our analysis to clouds located beyond 40 kpc from the center of the host galaxy, which we define as the edge of the ISM in Section 2.2 (this means the central position of the cloud is beyond 40 kpc). These choices for the linking length and minimum particle number ensure that the total mass of the identified clouds matches the total mass of cold gas particles ($T < 3 \times 10^4$ K) beyond 40 kpc, thereby providing a complete and consistent accounting of the cold gas in the outer CGM.

In Figure 2, we present the distribution of cloud radii and masses across three time bins up to 1.5 Gyr, with left and right panels corresponding to the m09 and m10 runs, respectively. Each panel also includes 1D histograms along the top and right axes, representing the mass and radius distributions, respectively. The plotted data include all cold clouds identified in each snapshot within a given time bin (50 snapshots per bin). As a result, some clouds appear multiple times in a panel because they persist across multiple snapshots.[13]

In the first time bin, the majority of the identified cold clouds are associated with the satellites, based on their consistency in both mass and size with the satellite properties. For reference, the m09 satellite has a gas mass of $7 \times 10^7\, M_\odot$ and a gas disk radius of 0.87 kpc, while the m10 satellite has a

[13] We also show and discuss the cloud properties from individual snapshots for the 0.5 Gyr and 1 Gyr outputs in Figure 11 and Appendix B, and find consistent trends.

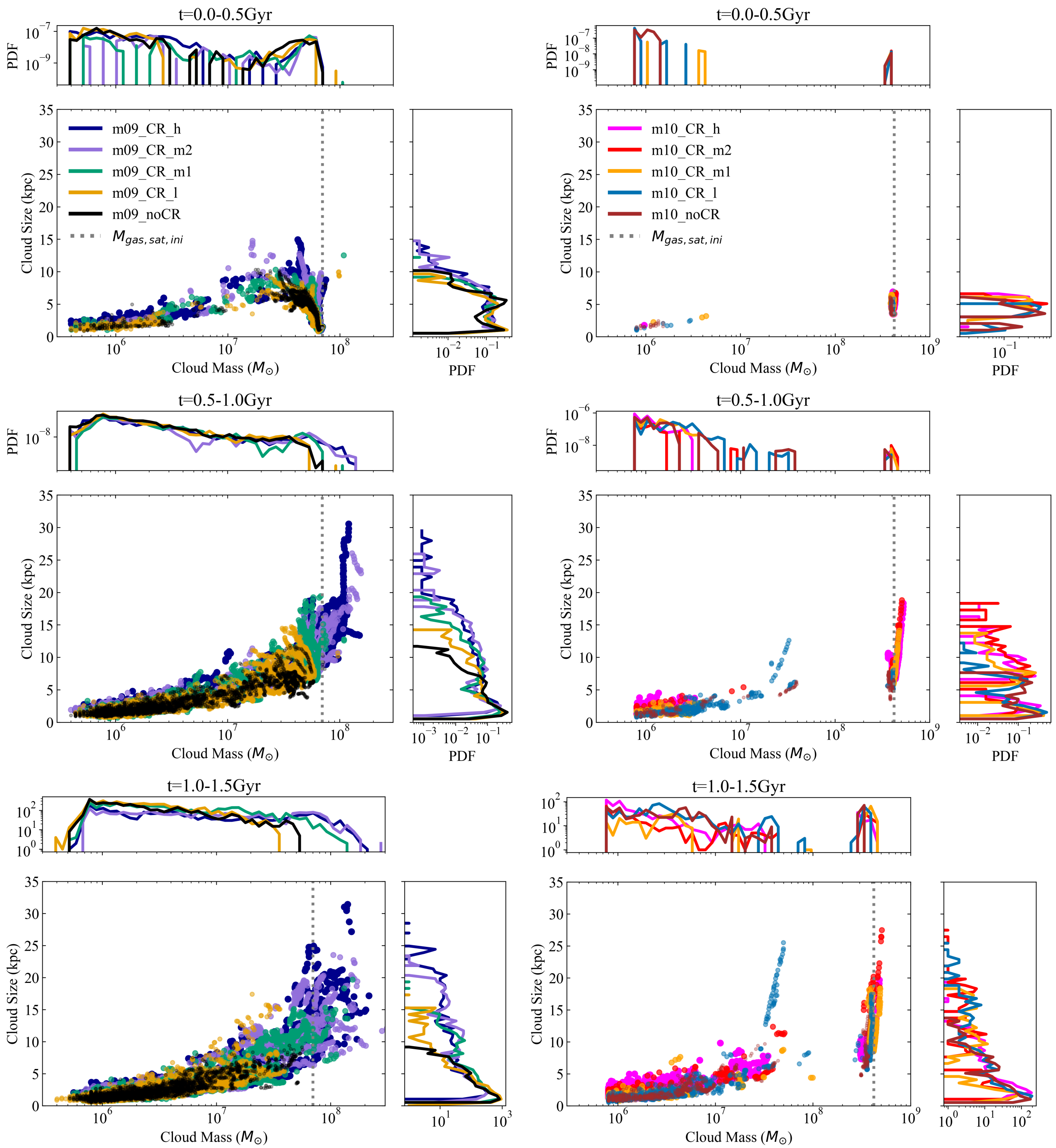

Figure 2. Size and mass distributions of cold gas clouds identified using the Friends-of-Friends (FoF) algorithm across three time bins up to 1.5 Gyr (top to bottom rows). The left and right panels correspond to the m09 and m10 simulations, respectively. Each panel includes one-dimensional histograms along the top and right axes, showing the distributions of cloud mass and size, respectively. Cold clouds are defined using a temperature threshold of $T < 3 \times 10^4$ K and identified using a linking length of 2 kpc with a minimum group size of 10 particles. CRs enhance the formation of larger, more coherent cold gas clouds by suppressing fragmentation and enabling their long-term survival and growth through enhanced mixing-layer cooling.

gas mass of $4.2 \times 10^8\,M_\odot$ and a gas disk radius of 2.1 kpc. In the m10 cases, the clouds are more clearly associated with the satellites, as relatively little gas has been stripped by 0.5 Gyr. However, we observe a smoother distribution of cloud masses and sizes in the m09 runs, likely due to the earlier onset and more rapid stripping in those runs.

Initially, there is no significant difference between the no-CR and CR runs. At later times (the lower two rows), stripping and fragmentation become more prominent, leading to an increasing number of lower-mass and smaller clouds in all runs. In the intermediate time bin, particularly for the m09 runs and, to a lesser extent, for the large clouds ($>10^8\,M_\odot$) in the m10 runs, we observe a monotonic increase in cloud size with increasing CR content: Higher CR levels produce systematically larger clouds. The largest clouds in the high-CR runs exceed those in the no-CR runs by about 10–15 kpc in radius. Additionally, the number of fragmented, low-mass clouds is also slightly lower in the high- (`h`) and mid- (`m2`) CR simulations than in the other cases. This effect is more visible in the m09 run.

CRs provide additional pressure support to the clouds, making them puffier and less dense. In the high-CR run, the cold gas fraction in the CGM with a density below 10^{-3} cc^{-1} is ∼24%, whereas it is only 0.3% in the no-CR case. The additional CR pressure can puff up the stripped gas. Also, unlike thermal energy, CR energy is less susceptible to radiative cooling losses. Therefore, when CR pressure dominates, reductions in thermal pressure due to cooling do not result in significant gas compression. Instead, the gas cools isochorically (at constant volume) rather than isobarically (at constant pressure), as is typical for thermally unstable gas, where cooling leads to density enhancements. Therefore, as a result of this isochoric cooling, high CR pressure tends to produce larger, lower-density cold clouds (I. S. Butsky et al. 2020; S. Ji et al. 2020).

In terms of mass, the most massive clouds in the no-CR and low-to-mid (`m1`) CR runs do not exceed the initial gas mass of the satellites (indicated by the vertical gray dotted line). In contrast, the high- and mid- (`m2`) CR runs produce clouds with masses reaching roughly ∼2 times the initial satellite gas mass. This growth can be attributed to the increased surface area of the larger clouds, which enhances mixing with the ambient medium. The mixing layers facilitate cooling, allowing the clouds to grow further and persist for longer durations. Notably, the cloud radii also increase by a factor of 2, directly implying lower densities (M/r^3) in the CR runs compared to the no-CR case.

In the final time bin, the physical processes described above continue to produce distinct cloud populations in the no-CR versus CR runs. The clouds in the no-CR run tend to have lower masses and smaller sizes than at earlier times, indicating that they are highly fragmented, likely due to significant disruption and mixing with the ambient medium. In contrast, the CR runs retain larger and more coherent cloud structures, with the high-CR case preserving the most intact and extended cold gas clouds. This highlights the role of CR pressure in stabilizing stripped cold gas against fragmentation over longer timescales. To approximately compare cloud survival times in our simulations, we compute the cloud-crushing times following Equation (2) of M. Roy et al. (2024). Consistent with expectations, larger clouds exhibit longer cloud-crushing times. As a result, the high-CR case shows cloud-crushing times of approximately 3–4 Gyr, roughly 2–3 times longer than those in the no-CR case (1–1.5 Gyr).

In summary, CRs promote the formation of larger and more coherent cloud structures, suppressing fragmentation and enhancing cloud survival. This behavior arises because CR pressure prevents isobaric collapse by enabling isochoric cooling. Consequently, the high-CR runs form puffier, lower-density clouds that grow and persist via enhanced mixing-layer cooling enabled by their larger surface areas. By the final time bin, the high-CR clouds remain relatively intact, whereas the no-CR clouds are heavily fragmented.

3.3. Do Cosmic Rays Affect the Cold Gas Mass Contribution from Satellites?

A natural follow-up question is whether the large, stripped cold gas clouds contribute significantly to the overall cold gas budget in the CGM. In this section, we examine whether CRs influence the total cold gas mass in the CGM that originates from satellite galaxies. Figure 3 shows the time evolution of cold gas mass beyond 40 kpc. The top-left panel includes all cold gas outside this radius: gas stripped from satellites, cold gas residing within satellites, and cold gas formed via induced cooling of host halo gas (corresponding to the sum of middle and bottom panels in Figure 3). The right panel, by contrast, excludes cold gas inside satellites and accounts only for stripped material and host gas that has cooled outside the satellite boundary (summed from the right-middle and right-bottom panels in Figure 3).

For the m09 run, we observe a clear trend of increasing total cold gas mass with increasing CR pressure (top panel). However, the difference between the no-CR and low-CR runs is relatively modest. In contrast, the m10 simulations exhibit minimal differences between the CR and no-CR runs at late times, and the total cold gas mass appears largely insensitive to the level of CR pressure among the CR runs. A similar trend holds for the total CGM cold gas mass. Notably, around 1 Gyr, the total cold gas mass in the CGM for the high-CR case is ∼4 times greater than that in the no-CR run.

To better understand the contribution of each component to the cold gas budget, we now investigate which component (classified into categories in Section 2.1) is most affected by the presence of CRs. The middle-left panel of Figure 3 shows the evolution of cold gas inside satellites (category: sat), revealing that the stripping timescale is generally longer in CR runs compared to the no-CR case. Interestingly, however, we observe a nonmonotonic trend with CR fraction. In the m09 case, the high-CR run exhibits the most rapid stripping (within ≲1 Gyr), followed by the mid-CR run (∼1 Gyr), while the low-CR run exhibits the slowest stripping rate (extending beyond 1 Gyr). However, these differences in mass are small and not significant given the mass resolution of our simulations. Despite the faster stripping in the high-CR case, the stripped gas (category: sat −> host) remains in the CGM for a longer duration, as seen in the sustained cold gas mass in the middle-right panel of Figure 3. This persistence may indicate longer cloud survival times, as discussed further in Section 3.5.

The bottom two panels of Figure 3 display the evolution of induced cooling in the host CGM, distinguishing between gas cooled inside (bottom left; category: host −> sat) and outside (bottom right; category: host) of the satellite boundaries. In both cases, we find a clear trend: Stronger CR pressure leads to enhanced cooling of the host gas. The cooling of the host gas inside satellites increases monotonically with CR strength in the m09 run. Similarly, for gas that cools outside the satellite, primarily due to mixing-layer processes, the high- and mid-CR runs show significantly more cold gas than the low-CR and no-CR cases. This enhanced mixing-layer cooling contributes substantially to the total cold gas content in the CGM, reinforcing the role of CRs in promoting cold gas growth beyond 40 kpc. The cold gas mass trends in the m10 runs are less pronounced but follow similar trends to the m09 runs.

In summary, CRs enhance the total cold gas mass in the CGM by affecting the contributions of stripped gas (middle-

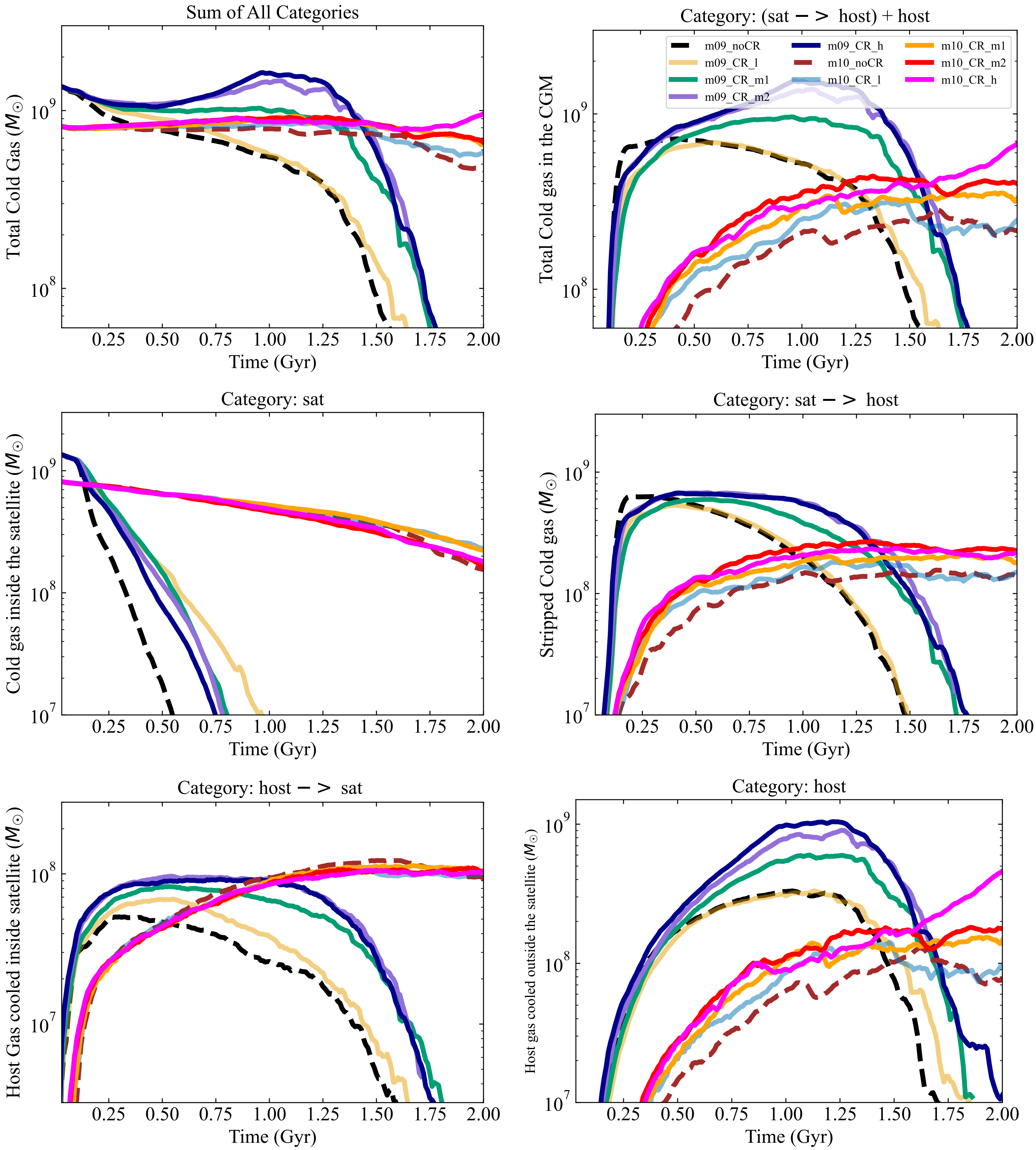

Figure 3. Time evolution of cold gas mass ($T \leqslant 3 \times 10^4$ K) beyond 40 kpc from the host-galaxy center, split into the four categories defined in Section 2.2. Middle left: cold gas inside satellites. Middle right: stripped cold gas. Bottom left: host gas cooled inside satellites. Bottom right: host gas cooled outside satellites. The top-left panel shows the total cold gas in the CGM and satellites (sum of the middle and bottom panels). The top-right panel shows the total cold gas in the CGM only, excluding satellite-bound gas (sum of the right panels in middle and bottom rows). Increasing CR pressure enhances the total stripped cold gas mass and promotes mixing-layer cooling, along with increasing the total cold gas mass, with the largest differences between the no-CR and high- (`h`) and mid- (`m2`) CR runs.

right panel of Figure 3) and mixing-layer cooled gas (lower-right panel of Figure 3). Higher CR pressure increases the longevity of stripped gas in the CGM. CRs also promote greater induced cooling of the host gas in the mixing layer. These effects collectively lead to a sustained and elevated cold gas reservoir in the CGM with increasing CR strength.

3.4. Do Cosmic Rays Affect the Covering Fraction of Cold Gas?

In this section, we examine the covering fraction of cold gas—an observable quantity that provides insight into the spatial distribution of the CGM. While direct quantitative

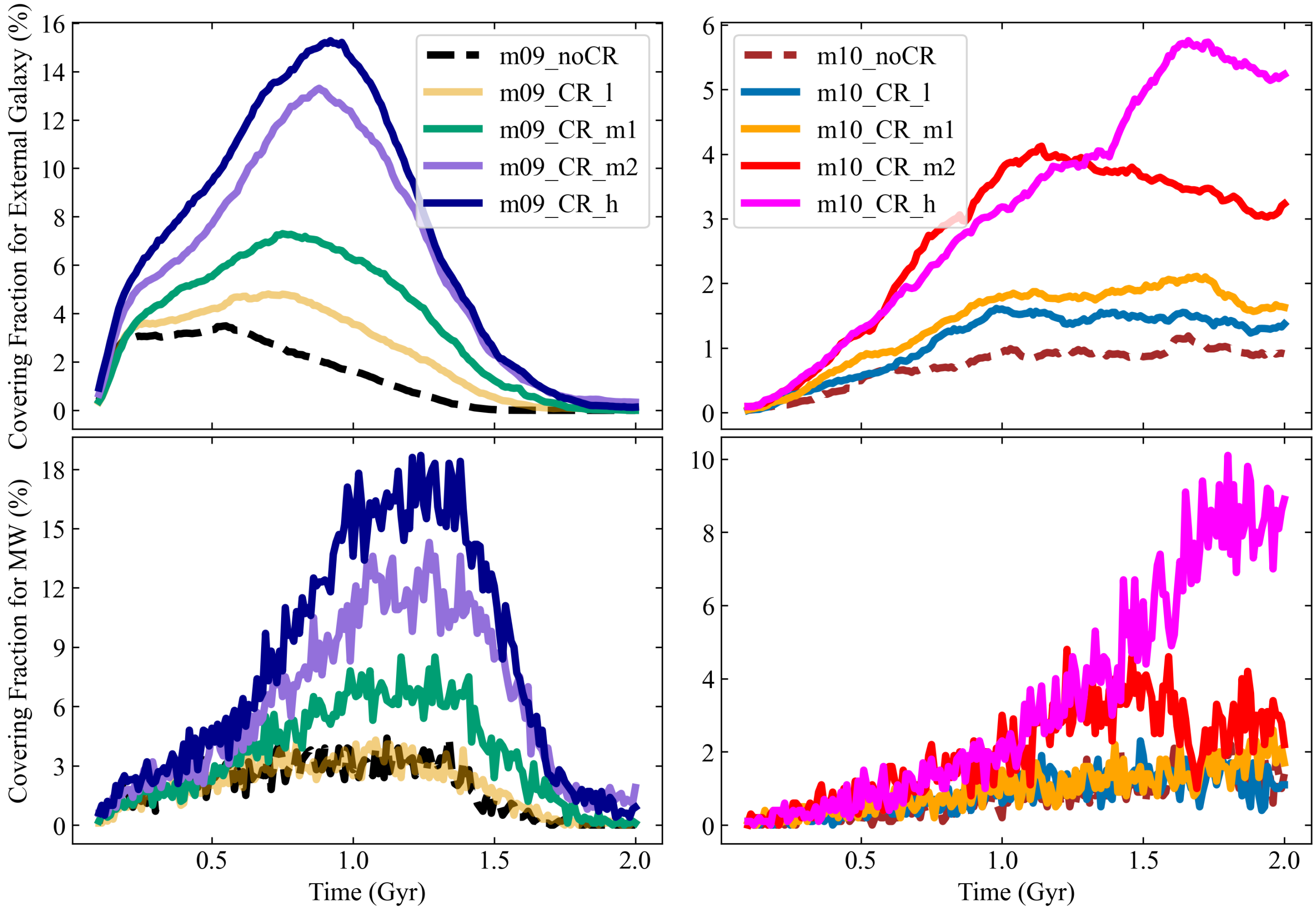

Figure 4. Covering fraction of cold gas ($T < 3 \times 10^4$ K) as a function of time for different CR strengths in the m10 (right panel) and m09 (left panel) runs. The bottom panels show the covering fraction for a Milky Way–like view, with sight lines originating from the galactic center, while the top panels represent an external galaxy view using parallel sight lines. In both geometries, the covering fraction increases with CR content, with the high-CR runs showing the most significant enhancement, reaching up to ∼5–6 times higher than in the no-CR case. The column density of cold gas exceeds 10^{18} cm^{-2} in all runs; thus, the covering fractions shown here correspond to $N > 10^{18}$ cm^{-2}.

comparisons with observations are important, they are not appropriate for our idealized setup with a simplified satellite distribution. Our goal is to study trends in observationally motivated quantities related to ram-pressure-stripped cold clouds and their dependence on CRs, rather than to make precise predictions for the MW covering fraction. Given that CRs tend to produce larger and more coherent cold gas clouds, we expect a corresponding increase in covering fraction with increasing CR content.

Since it is observationally challenging to distinguish between satellite-origin and host-origin gas, we compute the covering fraction by considering all cold gas particles with $T < 3 \times 10^4$ K located beyond 40 kpc, irrespective of origin. We calculate covering fractions for two viewing geometries: (1) an external observer viewing the galaxy from afar, and (2) an internal observer situated at the center of a MW-like galaxy. For the MW case, we sample 1000 random sight lines radially outward from the galactic center, spanning angles from $-180°$ to 180°. For the external view, we use 1000 randomly sampled parallel sight lines passing through the CGM (40 kpc $< r <$ 200 kpc).

Figure 4 shows the resulting covering fractions of cold gas for both geometries, with the top and bottom panels representing the external galaxy and MW views, respectively, for the m09 (left panel) and m10 (right panel) runs. We note that the covering fraction in the MW view is slightly higher than in the external galaxy view. This is primarily due to the radial nature of the sight lines. Additionally, the m09 runs, which contain a larger number of satellites than the m10 runs, exhibit greater covering fractions overall, as the increased number of stripped structures and easier-to-strip gas leads to broader spatial coverage in the CGM.

For the purposes of this work, the most important result is that the high-CR cases exhibit significantly larger covering fractions. The high-CR runs show covering fractions up to ∼5–6 times higher than those in the no-CR case for both the MW and external galaxy views. Focusing first on the m09 runs (left panels), we see a monotonic increase in covering fraction with increasing CR strength, although we highlight that the change becomes particularly dramatic only in the two highest-CR scenarios. The column density of a single cold gas particle exceeds 10^{18} cm^{-2} in all runs; thus, the covering fractions shown here correspond to $N > 10^{18}$ cm^{-2}. Increasing the threshold to 10^{19} cm^{-2} results in a modest decrease of ∼10% in the high-CR run, while the no-CR and low-CR runs show negligible variation. However, a realistic determination of the MW covering fraction would require including the observed satellite population and carefully modeling observational selection effects, which are beyond the scope of this work and are deferred to future studies. A similar trend holds for the m10 runs, though the overall covering fractions are lower. Again, the increase is most pronounced in the high-CR scenario, while differences among the no-, low- (l), and mid- (m1) CR runs remain modest.

Observations of the cold phase of the CGM in both the MW and external galaxies have revealed high covering fractions. For instance, J. M. Shull et al. (2009) report a covering fraction of 81% ± 5% for Si III high-velocity clouds (HVCs) along high-latitude Galactic sight lines. Similarly, N. Lehner & J. C. Howk (2011) find covering fractions of 50% and ⩽67% for intermediate-velocity HVCs (or iHVCs) in stellar and active galactic nuclei sight lines, respectively. In the case of external L^* galaxies, J. K. Werk et al. (2013) find a ∼70% covering fraction for Mg II within 75 kpc, while C. Thom et al. (2012), J. Tumlinson et al. (2013), J. K. Werk et al. (2013), and M. C. Wilde et al. (2021) report that the total covering fraction of cool gas can reach up to 80%–90% for H I column densities $N_{\rm HI} > 10^{14}\,{\rm cm^{-2}}$. While it comes as no surprise that our idealized insertion of a small number of satellites produces much lower covering fractions than observations, our results suggest that CRs can play a significant role in generating such high covering fractions. By promoting the formation of larger, more coherent cold gas clouds and suppressing fragmentation, CRs enhance both the spatial extent and survival of the cold phase. This leads to systematically larger covering fractions in our high-CR simulations compared to runs without CRs. CR-driven cloud growth and stabilization may therefore provide an important physical mechanism allowing for the high covering fractions observed in both the MW and external galaxies.

In summary, CRs enhance the covering fraction of cold gas in the CGM, with the effect being most pronounced in the high-CR runs. In the high-CR m09 case, the covering fraction increases by up to a factor of 8 relative to the no-CR scenario, underscoring the role of CRs in boosting the spatial visibility of cold gas. Thus, CRs may provide one possible explanation for the observed high covering fractions of cold gas. This effect is especially evident in the MW view because of the radial sight-line geometry, although it is also present in external galaxy projections.

3.5. Do Cosmic Rays Affect the Inflow Rate?

In this section, we assess whether the cold gas contributed by satellites is capable of feeding the central galaxy. We restrict our analysis to the m09 runs, as the stripping timescale for the m10 satellites exceeds 2 Gyr. We aim to answer two key questions: (1) What is the inflow rate of cold gas into the ISM? and (2) Can this cold gas supply the galaxy with sufficient material to sustain star formation?

Figure 5 presents the time evolution of the net mass flux (where negative values indicate inflow) of cold gas (defined as $T \leqslant 3 \times 10^4$ K).[14] The flux is computed across two spherical shells of 1 kpc thickness located at 80 kpc—where the satellites reside between 100 and 150 kpc (left panels)—and at 40 kpc, which defines the boundary between the CGM and the inner galaxy (right panels), from the galactic center. The top and bottom panels represent flux contributions from satellite-origin and host-origin cold gas, respectively. We show the instantaneous flux with light-shaded lines and the time-integrated flux with dark-shaded lines. We find that the instantaneous inflow rate increases with increasing CR pressure. For the time-integrated flux, the difference between the low-CR and no-CR runs is minimal, while the mid-CR runs exhibit higher fluxes than the no-CR case. In particular, the largest difference occurs in the mass flux across the 40 kpc shell—the boundary between the CGM and the inner galaxy—where, in the high-CR run, the peak instantaneous flux is enhanced by factors of ∼2 and 4 relative to the no-CR case for satellite-origin and host-origin gas, respectively. This suggests that CRs significantly facilitate the delivery of cold gas into the central galaxy.

Since the satellites are located between 100 and 150 kpc, cold gas begins to enter the 80 kpc shell earlier (∼0.6 Gyr), while it reaches the 40 kpc shell slightly later (∼0.8 Gyr), for both satellite-origin and host-origin gas. For satellite-stripped cold gas, the high-CR run shows a peak instantaneous inflow rate of 1.4 $M_\odot\,{\rm yr^{-1}}$ at 80 kpc, which slightly increases to 1.75 $M_\odot\,{\rm yr^{-1}}$ at 40 kpc, indicating that these clouds survive as they migrate inward. The flux of host-derived cold gas increases significantly from 80 to 40 kpc, suggesting that additional cooling within the mixing layers—amplified as the gas moves into denser regions—enhances the cold gas mass. The time-integrated cold gas mass flux from satellites at 2 Gyr remains nearly constant at $\sim 6 \times 10^8\,M_\odot$ between 80 and 40 kpc, suggesting limited cloud destruction. In contrast, the integrated inflow mass flux from cooled host gas at 2 Gyr increases substantially over the same radial range, from $\sim 10^9$ to $\sim 3 \times 10^9\,M_\odot$, indicating substantial cloud growth driven by cooling of the host gas. This behavior underscores the role of CRs in promoting both the survival and growth of cold gas clouds seeded by satellites and mixed with the ambient CGM.

However, previous studies have shown that CRs can suppress gas inflow by providing additional pressure support. For instance, I. S. Butsky et al. (2020) demonstrated that when the CR pressure is comparable to the thermal pressure ($P_{\rm CR}/P_{\rm g} \sim 1$), the mass-accretion rate can be reduced by nearly an order of magnitude. This suppression is not driven by a decrease in the cold gas mass fraction (i.e., cloud survival or destruction), but rather by a reduction in the inflow velocity due to enhanced CR pressure support against gravity, particularly in regions where the cooling time is long and CR pressure dominates. Similarly, K.-Y. Su et al. (2020) showed that even moderate CR pressure can suppress cooling flows through additional pressure support against gravity. C. W. Trapp et al. (2022) also found slightly lower mass fluxes in CR simulations than in the no-CR case. In contrast, our results indicate that CRs can enhance the inflow of cold gas into the central galaxy, particularly in the high-CR case, where we observe inflow rates up to 2–8 times higher than those in the no-CR run at 40 kpc. This enhancement arises from the increased survival of ram-pressure-stripped gas and the growth of cold gas through additional cooling of host halo gas within mixing layers, rather than from changes in the inward velocity. Our results therefore suggest a different mode of CR-regulated accretion in satellite-rich environments.

Given the high inflow rates of cold gas, we next examine whether this gas can effectively contribute to star formation in the host galaxy. To assess this, we analyze the star formation rate (SFR) evolution of the host galaxy, shown in the right panel of Figure 6. Light-shaded curves show the raw SFR time

[14] We exclude all cold gas originating from the central 40 kpc from our analysis, thereby removing any contribution from fountain flows.

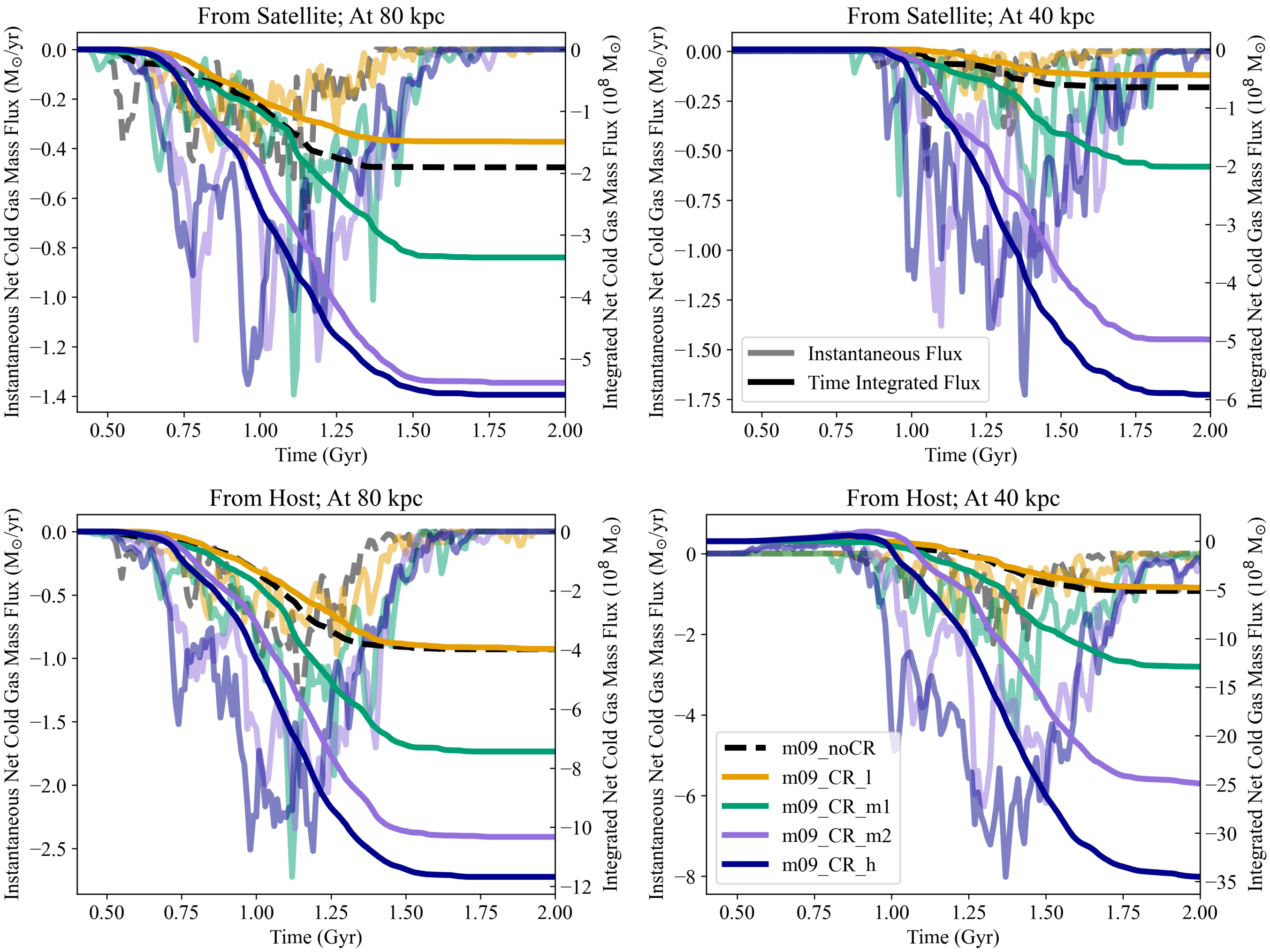

Figure 5. Time evolution of the net cold gas ($T \leqslant 3 \times 10^4$ K) mass flux for the m09 runs, measured across spherical shells of 1 kpc width located at 80 kpc (left panels) and 40 kpc (right panels), where negative values indicate inflow. Light-shaded lines indicate the instantaneous flux, while dark-shaded lines indicate the time-integrated flux. The top and bottom panels represent the mass flux contributions from satellite-origin and host-origin gas, respectively. Increasing CR content enhances the inflow of cold gas into the central galaxy, with the high-CR run exhibiting inflow rates approximately ∼2–4 times higher than those of the no-CR case.

series (displayed only for the no-CR, low-CR, and high-CR runs to avoid overcrowding the plot), while bold curves indicate smoothed trends based on a moving average. We find that the SFR in the CR runs exhibits greater temporal fluctuations than in the no-CR case. All CR runs show an early suppression of star formation up to 1.2 Gyr due to the additional CR feedback, consistent with previous studies (T. K. Chan et al. 2019; P. F. Hopkins et al. 2020; K.-Y. Su et al. 2020). While the average SFRs in the CR runs are comparable to (high-CR runs; h and m2) or lower than (low-CR runs; m1, l) those in the no-CR run at early times, the instantaneous SFR in the high-CR simulations occasionally reaches values 2–3 times higher than those in the other runs because of the larger temporal variability. However, at later times (∼1.2 Gyr), when the inflow rate becomes significantly enhanced in the high-CR runs, the degree of SFR burstiness and suppression decreases relative to the low-CR runs due to the sustained high influx of cold gas. The average SFR in the high-CR runs also increases to twice that of the no-CR run. We also plot the total cold gas mass flux at 40 kpc in the left panel of Figure 6. The high-CR run shows total net cold gas fluxes about a factor of 4 larger than those in the no-CR run, which aligns with the ratio of SFRs at later times. These results suggests that the large, coherent cold clouds supported by CR pressure not only survive infall but also deliver fuel to the galaxy, thus sustaining enhanced star formation.

In summary, CRs significantly enhance the inflow of cold gas into the central galaxy, with the high-CR run exhibiting inflow rates up to 2–8 times higher than those in the no-CR case at 40 kpc. This increased flux results from both the improved survival of satellite-stripped gas and additional cooling-driven growth of host gas within mixing layers. Due to the agreement between the mass flux and central SFRs in Figure 5, we argue that as this cold gas reaches the inner galaxy, it can fuel star formation. In particular, the high-CR run exhibits an increase in the average SFR at later times, despite the early suppression of star formation by CR feedback.

4. Discussion

4.1. What Drives Cloud Growth: Circumgalactic Medium Temperature or Cosmic Rays?

In this paper, we have found that CRs impact cloud survival and the multiphase structure of the CGM, and we have argued

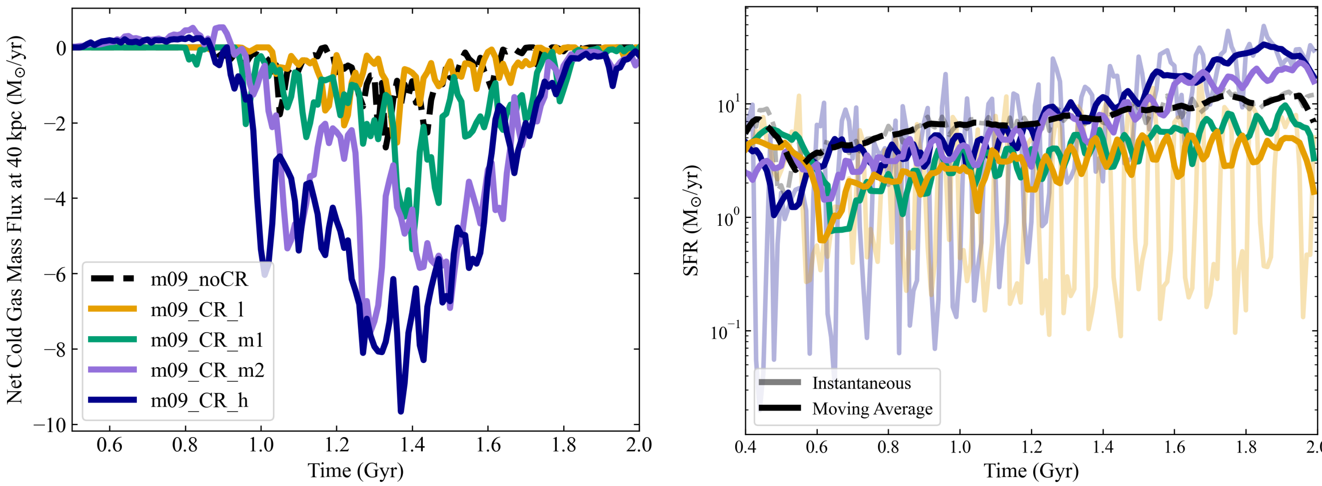

Figure 6. Left: total net cold gas flux at 40 kpc for the m09 simulations, where negative values indicate inflow. The total flux is obtained by summing the net flux components shown in the top-right and bottom-right panels of Figure 5. Right: star formation rate (SFR) of the host galaxy for different CR runs. Light-shaded curves show the raw SFR time series (displayed only for the no-CR, low-CR, and high-CR runs to avoid overcrowding the plot), while bold curves indicate smoothed trends based on a moving average. The CR runs display stronger temporal variability in SFR and can reach values up to twice those of the no-CR case. In the high-CR runs, the burstiness declines at later times because of the sustained influx of cold gas, unlike in the low-CR runs. Although the high-CR runs have average SFRs similar to the no-CR case at early times, their SFRs increase to roughly twice the no-CR value at later times, indicating that CRs enhance cold gas accretion and thereby feed central star formation.

that this is due to the direct influence of CR pressure on cloud properties. However, the cooling of the CGM and subsequent growth of cold clouds could also result from a cooler CGM, which would allow the mixing-layer gas to reach lower temperatures and cool more efficiently. To assess whether the observed cloud growth is primarily driven by CRs or by the associated reduction in the thermal pressure and temperature of the CGM, we use the `m09_CR_m2` simulation as our fiducial case. In this run, CR pressure constitutes one-quarter of the total pressure, thereby reducing the thermal pressure to three-quarters of its no-CR value. A plausible alternative explanation for the enhanced cloud growth is therefore that the lower thermal pressure (and hence lower CGM temperature, given the identical density profiles across our runs) promotes more efficient cooling in the mixing layer, leading to cloud growth.

To test this case, we perform three controlled variations of the fiducial run (described in the final three rows in Table 1). In the first, we restore the thermal pressure to its original no-CR value while retaining the CR component, resulting in a CGM that is overpressurized by 25% relative to hydrostatic equilibrium (`m09_CR_m2_overP`; shown in green). If the enhanced cloud growth were solely due to the reduction in thermal pressure, then no enhancement should occur in this case. However, as shown in the top panel of Figure 7, the cloud growth (green) remains qualitatively similar to that in the fiducial `m09_CR_m2` run (dark blue). We confirmed that the thermal pressure in the `m09_CR_m2_overP` case remains systematically higher than in the `m09_CR_m2` run throughout the evolution, while the overall cloud evolution remains comparable. In the middle panel, the stripping rate in `m09_CR_m2_overP` is somewhat higher than in `m09_CR_m2`, shifting the timescale for mixing-layer cooling (shown in the bottom panel), although the total amount of mixing-layer cooling remains comparable between the two runs. These results indicate that CRs directly contribute to cloud growth and survival.

In the second variation, we lower the thermal pressure to three-quarters of its no-CR value but exclude CRs, producing a halo that is underpressurized by 25% relative to hydrostatic equilibrium (`m09_noCR_underP`; shown in orange). If reduced thermal pressure alone were responsible for enhanced cloud growth, we would expect results similar to those of the fiducial CR run. Instead, as shown in the top panel of Figure 7, the resulting cloud population closely resembles that of the original no-CR run, with only a marginal increase in the size and mass of some clouds. This is consistent with the bottom panel, where the mixing-layer cooling is slightly greater than in the no-CR case, but still far weaker than in the fiducial CR run `m09_CR_m2`.

Finally, we test the effect of further reducing the thermal pressure in the fiducial CR run from three-quarters to one-half of the no-CR value, yielding a total pressure equal to that of the underpressurized no-CR run (`m09_CR_m2_underP`; shown in purple). This additional reduction only slightly increases the typical cloud size and mass and modestly prolongs the survival of mixing-layer gas relative to the fiducial CR run.

Overall, these tests demonstrate that, although reduced thermal pressure can contribute to modest cloud growth and extended survival, the dominant mechanism driving the substantial enhancement seen in our simulations is the direct influence of CRs.

4.2. Effects of Cosmic-Ray Transport: Variations in Diffusion Coefficient and Magnetic Field

In this section, we investigate whether CR transport affects cloud growth. The CR diffusion and advection timescales are given by

$$t_{\rm diff} = \frac{R^2}{D} \approx 30\ {\rm Gyr}\left(\frac{R}{100\ {\rm kpc}}\right)^2\left(\frac{D}{10^{29}\ {\rm cm^2\ s^{-1}}}\right)^{-1},$$

$$t_{\rm adv} = \frac{L}{v} \approx 0.98\ {\rm Gyr}\left(\frac{L}{100\ {\rm kpc}}\right)\left(\frac{v}{100\ {\rm km\ s^{-1}}}\right)^{-1}.$$

These scalings illustrate that diffusion is significantly slower compared to advection unless the diffusion coefficient is

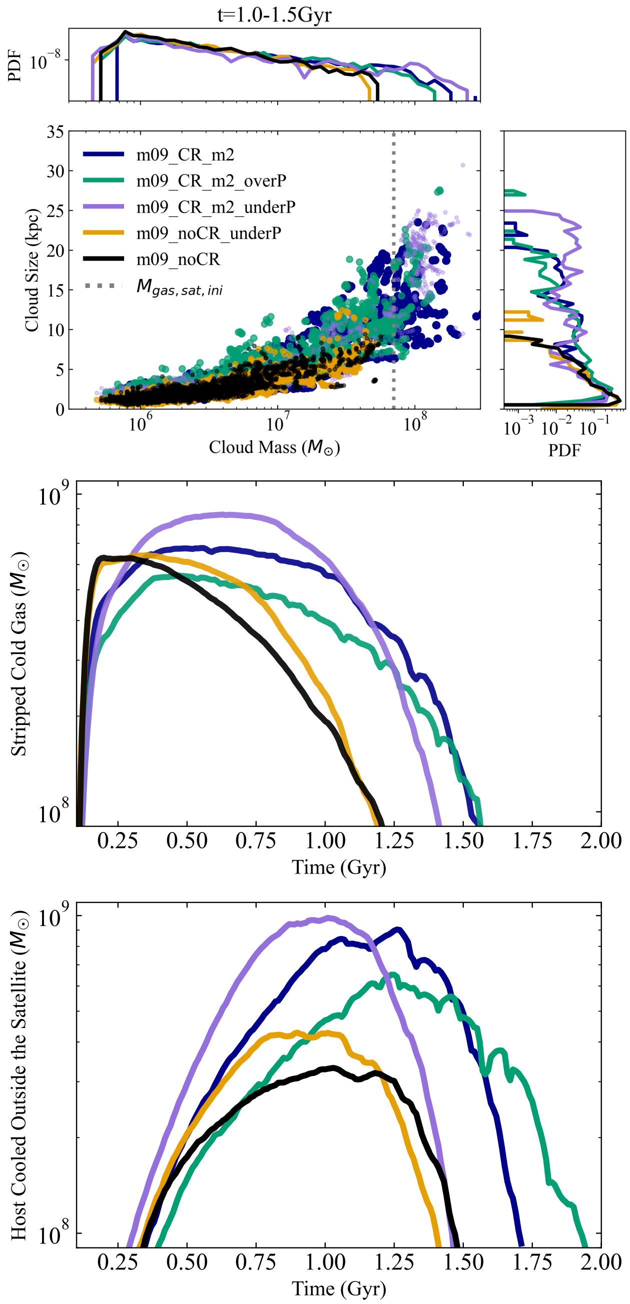

Figure 7. Cloud growth and mixing-layer cooling tests designed to isolate the effects of reduced thermal pressure from those of CRs. Top: cloud size and mass distributions for the fiducial CR run (`m09_CR_m2`; dark blue), overpressurized CR run (`m09_CR_m2_overP`; green), underpressurized no-CR run (`m09_noCR_underP`; orange), and low-thermal-pressure CR run (`m09_CR_m2_underP`; purple). Middle: time evolution of the stripped gas mass. Bottom: time evolution of mixing-layer cooling. The `m09_CR_m2_overP` case shows cloud growth similar to the fiducial CR run, indicating that CRs drive the enhancement independent of thermal pressure reduction. The `m09_noCR_underP` case shows only modest increases over the no-CR baseline, confirming that reduced thermal pressure alone cannot reproduce the CR-driven effect. Further lowering the thermal pressure in the CR run slightly increases cloud size and prolongs mixing-layer gas survival, but the dominant influence remains the presence of CRs.

extremely large. For CRs injected at the center of the galaxy, diffusion alone is insufficient to transport them to distances of $\sim$100 kpc within a Hubble time, unless $D \gg 10^{29}\,\mathrm{cm^2\,s^{-1}}$. Advection, by contrast, can reach such distances on billion-year timescales for typical outflow velocities. However, this timescale is still comparable to, or longer than, the timescale over which satellites experience significant ram pressure stripping according to our simulations. Consequently, in simulations with very low initial CR pressure, the contribution from centrally injected CRs does not arrive in time to meaningfully affect the satellite environment (we note that CRs injected at the accretion shock could reach outer satellites, but they would require similarly long timescales to reach radii of 100 kpc). This explains the minimal CR impact observed in such low-CR scenarios. While CRs are also injected by star-forming satellites, we find that their contribution is limited due to their low SFRs. Thus, local CR injection from satellites associated with star formation alone is unlikely to dominate the dynamics, unless additional CRs are injected by the black hole and/or the bow shock, which we plan to explore in future work. Therefore, the effect of CR energy density is dominant over the CR feedback from the host and satellite.

Our simulations initialized with higher CR pressure, however, show a pronounced impact on satellite gas stripping, consistent with CRs providing additional pressure support and modifying mixing and cooling in the cloud–wind interface. Given the uncertainties in CR transport, we further explore this regime by rerunning our high-CR model with reduced diffusion coefficient and with a lower β (i.e., a stronger magnetic field). Since CR streaming proceeds at approximately the Alfvén speed, a higher β corresponds to more efficient CR transport.

We find that the run with a lower diffusion coefficient, $D \sim 10^{28}\,\mathrm{cm^2\,s^{-1}}$, exhibits reduced survival of stripped cold gas (the difference in the solid lines) and less mixing-layer cooling (the difference in the dashed lines) compared to our fiducial CR run with a higher diffusion coefficient (right panel of Figure 8). With lower diffusion, CRs are transported less efficiently into the clouds, reducing their impact. In Figure 9, we show the time evolution of the median ratio of CR to thermal pressure both inside the clouds and in the surrounding background medium.[15] We find that the CR-to-thermal pressure ratio within the cloud is typically 2–4 times higher than in the surrounding CGM, and that this ratio also increases with time. The CR pressure increases toward the central regions, leading to a stronger CR background in the inner halo. As cold clouds fall inward, they encounter this increasingly CR-rich environment, allowing CRs to diffuse into the clouds from the surrounding medium and thereby enhance their internal CR content. The seemingly lower CR fraction in the background medium is primarily a consequence of its higher temperature. Since the background gas retains a large thermal energy reservoir, the ratio of CR to thermal pressure remains relatively small. In contrast, the clouds lose a significant fraction of their thermal energy, making the CR component comparatively more important within them. While the background CGM pressure ratio remains largely unchanged across these runs, the low-diffusion run exhibits systematically smaller $P_{\mathrm{CR}}/P_{\mathrm{th}}$ values inside the clouds than either of the fiducial diffusion runs. As a result, reduced diffusion leads to smaller cloud sizes and lower cloud masses relative to the fiducial CR run. The left panel of Figure 8 shows the distribution of cloud sizes and masses, indicating that in the

[15] We compute the median pressure ratio for all particles associated with clouds. To estimate the background value, we calculate the median pressure ratio using only particles not associated with clouds, evaluated at the radial positions of the cloud particles.

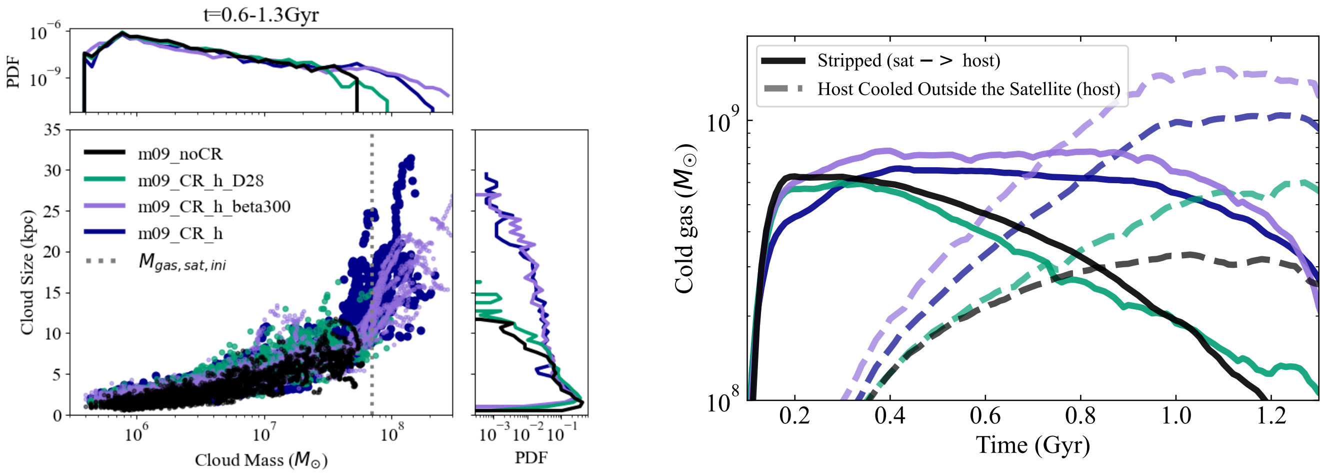

Figure 8. Illustration of the role of CR transport in regulating cloud survival and mixing in the halo. We show the variation in diffusion coefficient and magnetic field with our fiducial high-CR run. The left panel shows the cloud size–mass distribution at late times, while the right panel shows the time evolution of the stripped and mixing-layer cold gas mass. A high CR pressure alone is insufficient; efficient CR transport via a high diffusion coefficient and/or a strong magnetic field is also required for CRs to become dynamically important. The effect is more sensitive to the diffusion coefficient than to the magnetic field strength.

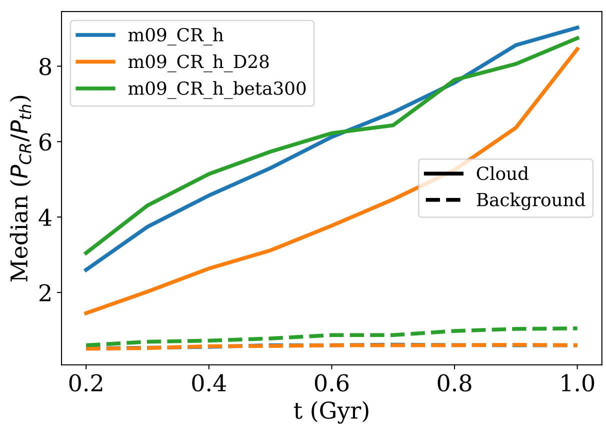

Figure 9. Ratio of CR to thermal pressure, inside and outside of the clouds for different runs. The blue dashed line is directly under the orange dashed line.

low-D case, CRs do not significantly inflate the clouds relative to the no-CR run, resulting in only modest size increases. Nevertheless, enhanced cooling in the mixing layer still promotes some cloud mass growth compared to the no-CR case.

From an observational perspective, T. K. Chan et al. (2019) showed that $D \sim 3 \times 10^{29}\,\mathrm{cm^2\,s^{-1}}$, or slightly lower values, are required to reproduce the observed γ-ray luminosities of L_* systems. Similarly, M. Roy & B. B. Nath (2022) found that the γ-ray luminosity observed in both the disk and extended ($\sim$100 kpc) halo of M31 can only be explained if $D \gtrsim 10^{29}\,\mathrm{cm^2\,s^{-1}}$. Consequently, $D \sim 10^{28}\,\mathrm{cm^2\,s^{-1}}$ is lower than the values inferred for the ISM by T. K. Chan et al. (2019), given the current γ-ray constraints. We also do not explore diffusion coefficients substantially higher than $3 \times 10^{29}\,\mathrm{cm^2\,s^{-1}}$, since such values would imply unphysically rapid CR transport across the halo, again inconsistent with the γ-ray constraints discussed by T. K. Chan et al. (2019). Although a diffusion coefficient of $10^{28}\,\mathrm{cm^2\,s^{-1}}$ is not physically motivated by current γ-ray observations, we use it to highlight the role of CR transport by varying D by an order of magnitude relative to our fiducial value.

The impact of CR transport is further illustrated in our high-magnetic-field run, in which we adopt an initial $\beta = 300$ (the ratio of thermal to magnetic pressure) while keeping the fiducial diffusion coefficient fixed. As shown in the right panel of Figure 8, this run exhibits survival of stripped gas comparable to the low-B fiducial case (solid line), but with enhanced mixing-layer cooling (the difference in the dashed lines). The left panel shows that the cloud size distribution remains similar to that of the low-B runs, although the clouds may be slightly more massive in the high-B case. This suggests that, unlike earlier simulations without CRs (e.g., T. A. Rintoul et al. 2025), where magnetic draping suppresses mixing, the inclusion of CRs may introduce a competing effect that changes the outcome.

Overall, we find that more efficient CR transport (high D or low β) leads to greater CR pressure within the clouds and consequently produces stronger mixing-layer cooling and longer survival of ram-pressure-stripped cold gas, as also demonstrated in the main text where we explicitly vary the CR fraction. These results again underscore the importance of CR transport in shaping cloud evolution. Therefore, not only is a high CR fraction in the halo required, but efficient CR transport (high diffusion coefficient and/or high magnetic field) is also necessary for CRs to become dynamically important in regulating cloud survival and mixing. Our results further indicate that this dependence is more sensitive to the diffusion coefficient than to the magnetic field strength. We will investigate the impact of CR transport on the CGM in more detail in future work.

4.3. Limitations of This Work

We note several limitations of our setup. First, our simulations are idealized and do not include a cosmological context; in particular, they lack cosmological accretion and large-scale evolution, both of which could drive additional turbulence and supply cold gas to the outer halo. Second, our satellite configuration is simplified and does not reflect the actual distribution of MW satellites, although the satellite mass range we adopt is broadly consistent with that observed in the MW. Finally, CR transport in the CGM remains highly uncertain due to limited observational constraints, and these uncertainties are compounded by the poorly constrained CGM magnetic field, since CR transport and energy losses depend sensitively on its properties. We address the uncertainty associated with CR transport in Section 4.2. Another limitation of our study is the adoption of a single energy bin corresponding to ∼GeV CR protons. Explicit modeling of lower-energy (∼MeV) CRs could alter the ionization balance and thermal phase structure of the gas; we defer such an investigation to future work. We also note that we employ the two-moment method used by T. K. Chan et al. (2019), which is motivated by the M1 method in radiation hydrodynamics. This approach replaces the commonly used single-moment, spectrally integrated CR diffusion–advection equation with an isotropic CR closure. More recently, newer two-moment methods (e.g., P. F. Hopkins et al. 2022; T. Thomas & C. Pfrommer 2022) have been shown to provide improved accuracy across all scales. However, implementing these methods is not expected to significantly alter the large-scale physics (P. F. Hopkins 2025). We plan to explore these updated two-moment methods, along with multibin CR spectra, in future work.

5. Conclusion

In this work, we explore the role of CRs in shaping the cold phase of the CGM, focusing specifically on ram-pressure-stripped gas from satellite galaxies in a MW-like environment using idealized simulations. Our key findings are summarized below:

1. *CRs alter cloud morphology.* CR pressure causes ram-pressure-stripped cold gas clouds to become more extended and diffuse (puffier), increasing their surface area and suppressing fragmentation (Figures 1 and 2).
2. *Enhanced mixing-layer cooling.* The larger surface area of CR-inflated clouds facilitates more efficient mixing with the surrounding hot CGM, leading to enhanced cooling and cloud mass growth (Figures 2 and 3).
3. *Higher cold gas budget.* The total cold gas mass in the CGM is up to 4 times higher in the high-CR runs than in the no-CR runs, particularly around the epoch of satellite stripping (Figure 3).
4. *Greater covering fractions.* CRs produce larger and more coherent clouds, increasing the sky covering fraction of cold gas, with high-CR runs showing covering fractions up to 5–6 times larger in both external and MW views (Figure 4).
5. *Increased cold gas inflow.* The enhanced growth and survival of cold clouds in CR-rich environments result in significantly higher inflow rates into the central galaxy—up to 2–8 times greater than in the no-CR case at 40 kpc (Figure 5).
6. *Boosted star formation.* The enhanced cold gas supply in the CR runs drives an approximately 2 times increase in both the instantaneous and time-averaged SFR at late times, particularly in the high-CR scenarios (Figures 5 and 6).

In conclusion, our study demonstrates that CR-dominated ram-pressure-stripped clouds can evolve into significantly larger and more massive structures. Not only do we find that CRs in the CGM will enhance the cold gas content of the host halo, but they will also affect the central galaxy by increasing the cold gas inflow rate and therefore the SFR. Although we have focused on clouds stripped from satellites, we expect the effect of CRs on cold gas survival to apply more generally to clouds formed within, or injected into, the CGM through other mechanisms as well. Finally, our work highlights the importance of including physically realistic CR models in simulations of galaxy formation and evolution.

Acknowledgments

We thank Greg Bryan, Todd Thompson, Phil Hopkins, Peng Oh, Claude-André Faucher-Giguére, and the FIRE collaboration for useful discussions and suggestions. M.R. acknowledges support from the CCAPP fellowship at The Ohio State University and ACCESS allocations of PHY240003. M.R. acknowledges the Aspen Center for Physics and Simons Foundation, as part of this work was performed there, which is supported by a grant from the Simons Foundation (grant No. 1161654, Troyer). K.Y.S. acknowledges support from the Black Hole Initiative at Harvard University, which is funded by grants from the John Templeton Foundation and the Gordon and Betty Moore Foundation, and acknowledges ACCESS allocations TG-PHY220027 and TG-PHY220047 and Frontera allocation AST22010. K.Y.S. was also supported by NASA through grant Nos. 80NSSC22K1124 and 80NSSC24K1224. The computations in this work were run at facilities supported by the Bridges, University of Pittsburgh and Anvil, Purdue University.

Data Availability Statement

A public version of the GIZMO code is available at http://www.tapir.caltech.edu/~phopkins/Site/GIZMO.html. The full simulation output cannot be included due to the large size. The processed data underlying the figures in this article can be requested from the corresponding author for scientific use. Data will be provided via large-file transfer methods, typically through university-supported systems.

Appendix A
Convergence Test

We also performed higher-resolution (hr) runs, shown by the dotted lines in Figure 10. The mass resolution of the low-resolution (lr) runs is $4 \times 10^4\, M_\odot$ for m09 and $8 \times 10^4\, M_\odot$ for m12, while the hr runs use a mass resolution of $8 \times 10^3\, M_\odot$. We expect the hr runs to better resolve denser and colder gas than the lr runs. Upon initial inspection, we find that the cold gas mass in the hr runs is qualitatively similar to that in the lr runs and exhibits the same trends with satellite mass, indicating that our general results are robust to changes in resolution. In the hr runs, cold dense gas is initially more difficult to strip, resulting in a larger amount of stripped gas surviving for longer times compared to the lr runs in both the CR and no-CR cases (left panel). The mixing-layer cooling is also reduced in the hr runs relative to the lr runs at early times, as the hr runs allows smaller structures to be resolved, which are more easily disrupted than larger clouds with longer survival times (M. Gronke & S. P. Oh 2018; D. B. Fielding & G. L. Bryan 2022). However, at later times, the CR runs show similar levels of mixing-layer cooling in both the hr and lr runs, suggesting convergence in the CR runs. In contrast, the no-CR hr run continues to exhibit less mixing-layer cooling even at late times. This implies that increasing the resolution, even in the presence of only a small CR component, enhances mixing-layer cooling relative to the no-CR case, further strengthening our conclusions.

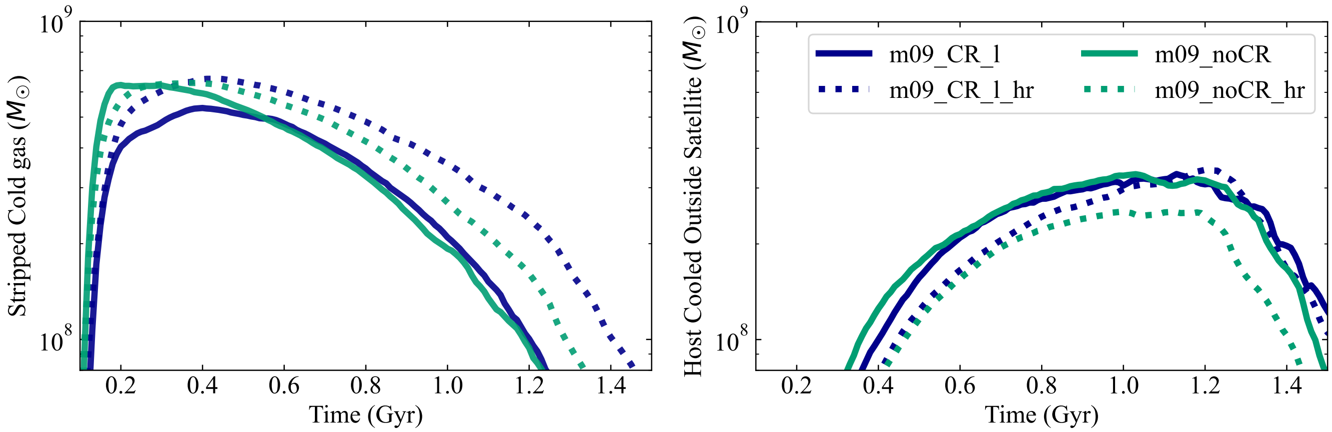

Figure 10. Left: mass of stripped cold gas from the satellite as a function of time for different resolution runs. Right: mass of host gas that cools outside the satellite in the same runs. Higher resolution enhances the stripping rate, but the qualitative trends and conclusions remain unchanged.

Appendix B
Cloud Properties in a Single Snapshot

We present the cloud size and mass distributions from individual snapshots at 0.5 and 1 Gyr in Figure 11. The overall trends are consistent with those obtained from the time-integrated analysis, indicating that our results are not driven by temporal averaging. However, the smaller number of clouds present in any single snapshot makes the differences between the runs less visually pronounced.

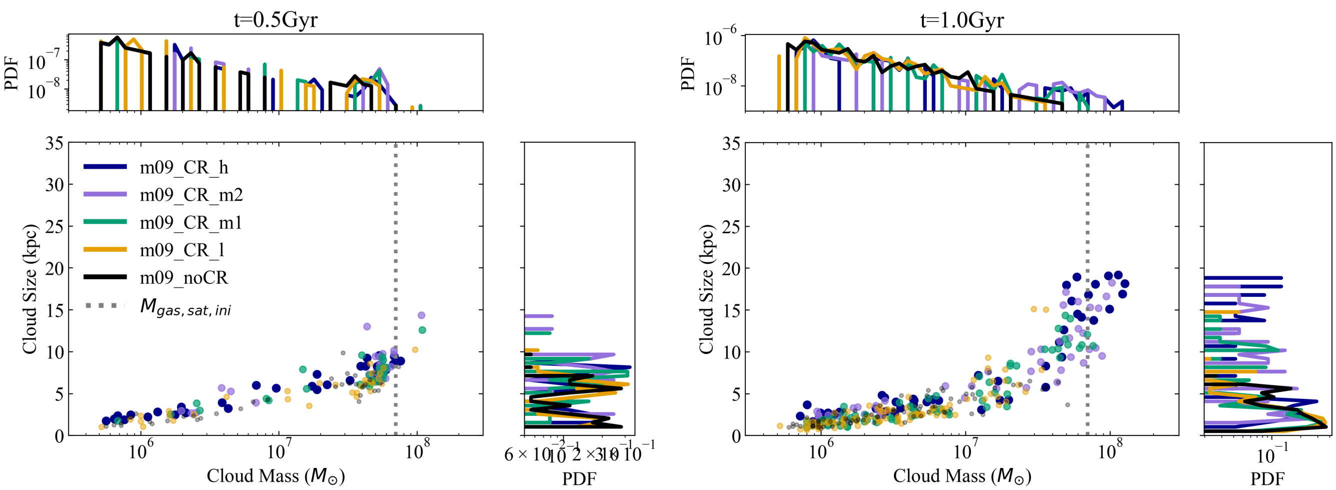

Figure 11. Size and mass distributions of cold clouds in individual snapshots across the two time bins used in Figure 2.

ORCID iDs

Manami Roy https://orcid.org/0000-0001-9567-8807
Kung-Yi Su https://orcid.org/0000-0003-1598-0083
Stephanie Tonnesen https://orcid.org/0000-0002-8710-9206
Yue Samuel Lu https://orcid.org/0009-0001-6243-0861
Cameron Hummels https://orcid.org/0000-0002-3817-8133
Sam B. Ponnada https://orcid.org/0000-0002-7484-2695

References

Ashley, T., Fox, A. J., Jenkins, E. B., et al. 2020, ApJ, 898, 128
Berg, M. A., Howk, J. C., Lehner, N., et al. 2019, ApJ, 883, 5
Butsky, I. S., Fielding, D. B., Hayward, C. C., et al. 2020, ApJ, 903, 77
Chan, T. K., Kereš, D., Hopkins, P. F., et al. 2019, MNRAS, 488, 3716
Damle, M., Tonnesen, S., Sparre, M., & Richter, P. 2025, ApJ, 986, 69
Faucher-Giguère, C.-A., & Oh, S. P. 2023, ARA&A, 61, 131
Fielding, D. B., & Bryan, G. L. 2022, ApJ, 924, 82
Fielding, D. B., Tonnesen, S., DeFelippis, D., et al. 2020, ApJ, 903, 32
Fluetsch, A., Maiolino, R., Carniani, S., et al. 2021, MNRAS, 505, 5753
Gronke, M., & Oh, S. P. 2018, MNRAS, 480, L111
Guo, F., & Oh, S. P. 2008, MNRAS, 384, 251
Hopkins, P. F. 2015, MNRAS, 450, 53
Hopkins, P. F. 2016, MNRAS, 462, 576
Hopkins, P. F. 2017, MNRAS, 466, 3387
Hopkins, P. F. 2025, OJAp, 9 doi:10.33232/001c.161465
Hopkins, P. F., Chan, T. K., Garrison-Kimmel, S., et al. 2020, MNRAS, 492, 3465
Hopkins, P. F., & Raives, M. J. 2016, MNRAS, 455, 51
Hopkins, P. F., Squire, J., & Butsky, I. S. 2022, MNRAS, 509, 3779
Hopkins, P. F., Wetzel, A., Kereš, D., et al. 2018a, MNRAS, 477, 1578
Hopkins, P. F., Wetzel, A., Kereš, D., et al. 2018b, MNRAS, 480, 800
Ji, S., Chan, T. K., Hummels, C. B., et al. 2020, MNRAS, 496, 4221
Keeney, B. A., Stocke, J. T., Pratt, C. T., et al. 2018, ApJS, 237, 11
Krause, M., Irwin, J., Wiegert, T., et al. 2018, A&A, 611, A72
Kravtsov, A. V. 2013, ApJL, 764, L31
Kroupa, P. 2002, Sci, 295, 82
Lehner, N., & Howk, J. C. 2011, Sci, 334, 955
Leitherer, C., Schaerer, D., Goldader, J. D., et al. 1999, ApJS, 123, 3
Li, M., & Tonnesen, S. 2020, ApJ, 898, 148
McCourt, M., Sharma, P., Quataert, E., & Parrish, I. J. 2011, MNRAS, 419, 3319
McKee, C. F., & Cowie, L. L. 1975, ApJ, 195, 715
Pfrommer, C., Pakmor, R., Schaal, K., Simpson, C. M., & Springel, V. 2017a, MNRAS, 465, 4500
Pfrommer, C., Pakmor, R., Simpson, C. M., & Springel, V. 2017b, ApJL, 847, L13
Rintoul, T. A., van de Voort, F., Hannington, A. T., et al. 2025, MNRAS, 543, 4321
Roy, M., & Nath, B. B. 2022, MNRAS, 514, 1412
Roy, M., Nath, B. B., & Voit, G. M. 2021, MNRAS, 507, 3849
Roy, M., Su, K.-Y., Mathur, S., & Stern, J. 2025, ApJ, 988, 71
Roy, M., Su, K.-Y., Tonnesen, S., Fielding, D. B., & Faucher-Giguère, C.-A. 2024, MNRAS, 527, 265
Sharma, P., McCourt, M., Quataert, E., & Parrish, I. J. 2012, MNRAS, 420, 3174
Sharma, P., Parrish, I. J., & Quataert, E. 2010, ApJ, 720, 652
Shull, J. M., Jones, J. R., Danforth, C. W., & Collins, J. A. 2009, ApJ, 699, 754
Springel, V. 2000, MNRAS, 312, 859
Springel, V., & White, S. D. M. 1999, MNRAS, 307, 162
Su, K.-Y., Hopkins, P. F., Hayward, C. C., et al. 2017, MNRAS, 471, 144
Su, K.-Y., Hopkins, P. F., Hayward, C. C., et al. 2019, MNRAS, 487, 4393
Su, K.-Y., Hopkins, P. F., Hayward, C. C., et al. 2020, MNRAS, 491, 1190
Thom, C., Tumlinson, J., Werk, J. K., et al. 2012, ApJL, 758, L41
Thomas, T., & Pfrommer, C. 2022, MNRAS, 509, 4803
Trapp, C. W., Kereš, D., Chan, T. K., et al. 2022, MNRAS, 509, 4149
Tumlinson, J., Peeples, M. S., & Werk, J. K. 2017, ARA&A, 55, 389
Tumlinson, J., Thom, C., Werk, J. K., et al. 2013, ApJ, 777, 59
Uhlig, M., Pfrommer, C., Sharma, M., et al. 2012, MNRAS, 423, 2374
Voit, G. M., Donahue, M., Bryan, G. L., & McDonald, M. 2015, Natur, 519, 203
Werk, J. K., Prochaska, J. X., Thom, C., et al. 2013, ApJS, 204, 17
Werk, J. K., Prochaska, J. X., Tumlinson, J., et al. 2014, ApJ, 792, 8
Wilde, M. C., Werk, J. K., Burchett, J. N., et al. 2021, ApJ, 912, 9
Zhang, D., Thompson, T. A., Quataert, E., & Murray, N. 2017, MNRAS, 468, 4801